Atomic resolution structures of the methane-activating enzyme in anaerobic methanotrophy reveal extensive post-translational modifications

Marie-C. Müller[1], Martijn Wissink[2], Priyadarshini Mukherjee[1], Nicole Von Possel[1], Rafael Laso-Pérez[8], Sylvain Engilberge[3,4], Philippe Carpentier[3,5], Jörg Kahnt[6], Gunter Wegener[1,7], Cornelia U. Welte[2], Tristan Wagner[1,4#]

[1] Max-Planck-Institute for Marine Microbiology, Celsiusstraße 1, 28359 Bremen, Germany.

[2] Department of Microbiology, Radboud Institute for Biological and Environmental Sciences (RIBES), Radboud University, Heyendaalseweg 135, 6525 AJ Nijmegen, The Netherlands.

[3] European Synchrotron Radiation Facility, 38043 Grenoble, France.

[4] Univ. Grenoble Alpes, CEA, CNRS, Institut de Biologie Structurale, 38044 Grenoble, France.

[5] Univ. Grenoble Alpes CEA CNRS, IRIG-LCBM UMR 5249, 38000 Grenoble, France.

[6] Max Planck Institute for Terrestrial Microbiology, Karl-von-Frisch-Strasse 10, 35043 Marburg, Germany.

[7] MARUM, Center for Marine Environmental Sciences, University of Bremen, 28359 Bremen, Germany.

[8] Biogeochemistry and Microbial Ecology Department, Museo Nacional de Ciencias Naturales (MNCN-CSIC), C. de José Gutiérrez Abascal, 2, 28006, Madrid, Spain.

[#]Correspondence: twagner@mpi-bremen.de

Abstract

Anaerobic methanotrophic archaea (ANME) are crucial to planetary carbon cycling. They oxidise methane in anoxic niches by transferring electrons directly to nitrate or metal oxides and alternatively to sulfate-reducing bacteria. Due to their physiological complexity, no ANME species have been isolated, hampering the biochemical investigation of the enzymatic processes involved in anaerobic methane oxidation. To study the methane-capturing enzyme of these microorganisms, we circumvented the isolation barrier by exploiting microbial enrichments of freshwater nitrate-reducing ANME-2d grown in bioreactors, and marine ANME-2c in syntrophy with bacterial partners. The crystal structures of their Methyl-Coenzyme M Reductases (MCRs), refined to true atomic resolution, provided the most precise image of the enzyme to date. Despite their physiological differences, these ANMEs have extremely conserved MCR structures, similar to homologs from methanogenic *Methanosarcinales,* rather than the phylogenetically distant MCR of ANME-1 isolated from Black Sea mats. The three studied MCRs are highly modified, with seven post-translational modifications. Among them was a novel 3(*S*)-methylhistidine on the γ-chain of both ANME-2d MCRs. Labelling with gaseous krypton did not reveal any internal channels that would facilitate alkane diffusion to the active site as observed in the ethane-specialized enzyme. Based on our data, the methanotrophic MCRs should follow the same radical reaction mechanism proposed for the methane-generating homologues. The described pattern of post-translational modifications underscores the importance of native purification as a powerful approach to discovering intrinsic enzymatic features in uncultivated microorganisms existing in nature.

42 Introduction

43 In light of climate change, studies about planetary methane fluxes have become increasingly
44 important due to the global impact of the greenhouse gas. In anoxic marine sediments, about
45 71% of biogenic methane is transformed into the less potent greenhouse gas CO_2 through the
46 process of anaerobic oxidation of methane (AOM)(1). The same is true in terrestrial and
47 freshwater systems, where AOM may account for up to 50% reduction in methane emissions
48 in freshwater wetlands(2). The only microorganisms capable of performing AOM without the
49 use of oxygen as a methane-activating agent are anaerobic methanotrophic archaea (ANME)(3,
50 4). All ANME groups have been found in marine sediments except ANME-2d(5, 6). Electrons
51 retrieved during the complete oxidation of methane can be transferred to sulfate-reducing
52 partner bacteria (e.g., *Desulfobacterota*), most likely through direct interspecies electron
53 transfer (DIET) via nanowires(7, 8). Reports proposed that some ANMEs performed non-
54 syntrophic AOM by coupling methane oxidation to Fe(III), Mn(IV), or humic substances
55 reduction(9-12). In addition, freshwater ANME-2d can reduce nitrate(13) or colonise
56 electrodes and generate electricity(14).

57 Despite their common ability to turn methane into CO_2, ANME-1 and ANME-2/ANME-3 are
58 phylogenetically distant. To understand their physiological differences, it is of utter importance
59 to investigate the fundamental molecular mechanism of AOM. Despite extensive efforts, the
60 gathered biochemical information on ANMEs is scarce due to the absence of any axenic
61 cultures. However, some laboratories have succeeded in obtaining enrichments of microbial
62 consortia(15-17), a strenuous process due to the extremely long doubling times of ANME. This
63 achievement can represent a turning point in deciphering how these microbes catabolise
64 methane and might inspire biotechnological applications.

65 Methane capture, the first reaction in AOM, has been proposed to be carried out by the Methyl-
66 coenzyme M reductase (MCR). Accordingly, the reaction would follow the reverse direction
67 of methanogenesis(18). In the proposed mechanism, the heterodisulfide, made of Coenzyme
68 M (HS-CoM) and Coenzyme B (CoB-SH), would react with methane to generate methyl-S-
69 CoM and free CoB-SH through a radical mechanism catalysed by the Ni-containing
70 tetrapyrrole cofactor F_{430}(19, 20). Methane conversion to methyl-S-CoM was previously
71 proved in the methanogenic enzyme from *Methanothermobacter marburgensis*(21) despite its
72 unfavourable thermodynamics (Gibbs free energy change of +30 $kJ.mol^{-1}$ of transformed
73 methane)(4). To perform this difficult process, ANMEs produce considerable quantities of
74 MCR, which is by far the most abundant cellular enzyme(18, 22, 23). In addition, a

75 thermodynamic pull allowing an immediate conversion of methyl-S-CoM should proceed,
76 leading to subsequent transformation to CO_2.

77 MCR quaternary structure consists of a dimer of heterotrimers $(\alpha\beta\gamma)_2$ harbouring the cofactor
78 F_{430} in each active site(20). The catalytic chamber and its close surroundings contain many
79 post-translational modifications (PTMs) that vary among different methanogens and are
80 located on the α-subunit. No correlation has been observed so far between the PTMs and
81 phylogeny. While for some PTMs the installation machinery has been resolved, their
82 physiological functions remain elusive(24-27). The structures of ten methanogenic MCRs have
83 yielded considerable information, highlighting conserved overall features(19, 28). In contrast,
84 the MCR structure from ANME-1 revealed unique traits, including a modified methylthio-F_{430}
85 cofactor, a cysteine-rich patch, and two different PTMs (*i.e.*, a C7-hydroxy-tryptophan and a
86 methionine sulfoxide)(29), corroborated by biochemical studies(18, 22).

87 The unique traits hint towards the presence of other unexpected features in ANME MCRs.
88 Acquiring snapshots of the phylogenetically different counterparts in ANME-2 and ANME-3
89 would stimulate applied research in methane mitigation. Attempts have been made to facilitate
90 structural studies of ANME MCRs, including successful recombinant expression of ANME-1
91 MCR and the Ethyl-CoM reductase (ECR) specialised to activate ethane from '*Candidatus*
92 Ethanoperedens thermophilum'(30). However, this approach is biased as the machinery for
93 generating and installing native F_{430} variants, species-specific PTMs, and dedicated chaperones
94 required for correct folding are absent in the recombinant host. Moreover, artefactual chimeric
95 assemblies have been observed between the native MCR from the methanogenic host and the
96 recombinant ANME-2 MCR-γ. Similarly, the cultivation-independent approach of
97 computational protein structure modelling exhibits biases as the process is guided by extracted
98 data from known models, but cannot predict the physiological cofactor, PTMs, and other
99 unknown important functional traits such as water networks and gas channels. As an
100 illustration, the native ECR harbours a dimethylated-F_{430} cofactor, a widened active site and
101 unique PTMs (N^2-methylhistidine, a S-methylcysteine at a position different to the
102 methanogenic one, and 3-methylisoleucine) that scaffold a gas channel connecting the active
103 site to the solvent, favouring alkane diffusion(23). Therefore, to explore the specific features
104 of alkane-capturing enzymes, the investigation of native systems still prevails, which is a
105 challenge in the case of non-isolated microbes such as ANMEs.

106 In this study, we purified MCRs directly from microbial enrichments dominated by ANME-2
107 to compare them with methanogenic and methanotrophic (ANME-1) homologues. The native
108 structures obtained at atomic resolution reveal the detailed architecture of the methane-
109 capturing enzyme, with the discovery of a novel PTM on the γ-subunit. These findings expand
110 our knowledge of this crucial carbon-cycling enzyme, highlighting the importance of studying
111 natural systems.

112

113 ## Results

114 **Isolation of the core catabolic enzyme MCR from freshwater and marine ANME-2**

115 Cultures containing an abundant population of ANME are rare due to the laborious enrichment
116 procedures and the long doubling time of these organisms. Successive breakthroughs in the
117 cultivation of ANME-2 species have enabled us to access freshwater and marine
118 representatives for studying differences between their MCRs through native protein
119 purification (Figure 1 and Supplementary Fig. S1). In all presented cases, the native protein
120 isolation was based on MCR tracking by following its intrinsic properties: the absorption
121 signature from the F_{430} cofactor and the typical pattern on denaturing gels (SDS-PAGE,
122 Supplementary Fig. S2).

123 Investigations were started on a relatively simplified system in which ANME-2d grew
124 independent of sulfate-reducing partners. Biological samples were retrieved from Ooijpolder
125 (Netherlands)(31, 32) and Vercelli rice fields (Italy)(14, 17) and cultivated in bioreactors for
126 >5 years, significantly enriching ANME-2d with nitrate as an electron acceptor. Metagenomic
127 analysis of the Ooijpolder samples directly obtained during sampling time showed a read-based
128 relative abundance of 28% '*Ca.* Methanoperedens sp.' BLZ2 (Supplementary Fig. S1)(33)
129 (further referred to as ANME-2d^{O}). In comparison, metagenomic analysis of the Vercelli rice
130 field enrichment sample showed a read-based relative abundance of 9% '*Ca.*
131 Methanoperedens' (Supplementary Fig S1), with the main strain '*Ca.* Methanoperedens'
132 Vercelli Strain 1(34) (further referred to as ANME-2d^{V}). Both samples were separately
133 processed for protein purification, starting from 17.5 g and 12.5 g of ANME-2d^{O} and ANME-
134 2d^{V} containing biomass and yielding 114 mg and 14 mg of the major MCR, respectively
135 (Figure 1).

136 Furthermore, the purification setup was tested on a microbial enrichment from a marine system.
137 Here, the original sample used to initiate the enrichment was collected from the Amon Mud
138 Volcano in the Mediterranean Sea at a depth of 1,120 m and a temperature of 14 °C. The
139 microbial enrichment, grown at 20 °C in batch serum bottles since 2003, mainly gathered
140 ANME-2c (with a relative abundance of 32 %) along with microbial partners based on 16S
141 rRNA gene sequencing(7)(Supplementary Fig. S1). The processed biomass of 3.21 g contained
142 the microbial mixture as well as inorganic particles, and a final quantity of 4.9 mg of MCR
143 could be extracted.

144 In all cases, the final purified MCR fractions subjected to UV/Vis spectroscopy presented a
145 peak at 425 nm due to the F_{430} cofactor in accordance with previous reports for methanogenic
146 MCRs (Supplementary Fig. S2b-c)(23, 35). While the final SDS-PAGE suggests a high sample
147 homogeneity in solution, we could not exclude a mixture of MCRs from different subspecies.
148 Therefore, we used the selective crystallisation process to isolate and identify a single variant
149 by X-ray crystallography.

150

151 **MCR shows a well-conserved overall architecture**

152 X-ray crystal structures were solved for MCR from ANME-2d^{O} and ANME-2d^{V} and models
153 were refined to a final resolution of 0.98 Å (Table 1). Both MCRs crystallised in a monoclinic
154 space group with similar unit cell dimensions. Despite the differences in the organisms and the
155 slight deviations in the crystallisation solution (see methods), both MCR models shared the
156 same crystalline packing (Supplementary Fig. S3). The observation suggests a very close
157 sequence identity that would maintain the surface contacts to establish the same crystal lattice.
158 This was confirmed after sequencing the MCR from the initial electron density, matching the
159 sequences derived from metagenomic data. MCRs from ANME-2d^{O} and ANME-2d^{V} are
160 structurally almost identical with a root mean square deviations (rmsd) of 0.09 Å (with an
161 overall of 2,186 aligned Cα), probably due to their high sequence identity (with an identity of
162 95.4, 97.2, and 95.6% for α, β, and γ, respectively),

163 The dataset obtained for the ANME-2c enrichment was also of sufficiently high quality to
164 unequivocally determine the sequence from the electron density map at a resolution of 1.34 Å.
165 The derived sequence perfectly matched the one of ANME-2c MCR from the metagenomic
166 data (Supplementary Fig. S4 and S5). Based on the crystal structure, MCR from ANME-2c
167 seems to form stable dimers (Supplementary Fig. S3), as pointed out by the PISA server

168 analyses (the dimer exhibiting a ΔG^{int} of −617.2 kcal.mol^{-1} and a ΔG^{diss} of 26.8 kcal.mol^{-1}.
169 Analyses performed on the 25th of November 2024). The dimeric interface is exclusively
170 formed by the interaction of the α-subunits, mainly via the C-terminal extension. The dimeric
171 state does not disturb the access to the active site. Due to the low quantities of MCR obtained
172 at the end of the purification and the slow growth of the consortium, we were unable to test
173 whether this dimeric arrangement reflects a crystallisation artefact or a stable entity in solution.
174 Further studies will need to be carried out. On the other hand, the predicted trimeric
175 arrangement of the MCR from ANME-2d^{O} observed in blue native PAGE(33) was not detected
176 in the crystal structure. Nevertheless, we cannot exclude that the purification and crystallisation
177 process might have disrupted a trimeric organisation occurring *in vivo*.

178 Despite the different environmental niches, the marine ANME-2c and freshwater ANME-2d
179 MCRs have high amino acid sequence identities of 63.6, 61.5, and 71.4% for α, β, and γ subunit,
180 respectively (Supplementary Fig. S5-6). The overall structure of the three ANME-2 MCRs
181 matches that of the different methanogenic MCRs, of the methanotrophic ANME-1 MCR, and
182 of the ECR from '*Ca.* E. thermophilum' (Figure 2, Supplementary Fig. S5-6), the closest
183 homolog being the MCR from *Methermicoccus shengliensis*(35). Besides the overall
184 similarity, notable structural differences are summarised in Figure 2. The electrostatic profile
185 of the surface is also similar to previously studied MCRs, with both ANME-2d members
186 exhibiting more pronounced positive charges at the entrance leading to the active site than a
187 typical methanogenic MCR (Supplementary Fig. S7).

188

189 **A sealed, strictly conserved catalytic chamber covered by seven post-translational**
190 **modifications**

191 The active site of the three ANME-2 MCRs is highly conserved across all described MCRs
192 from methanogenic archaea and contains a canonical F_{430} cofactor in accordance with previous
193 studies(22) (Figure 3, Supplementary Fig. S8). The subatomic resolution of both ANME-2d
194 structures enables the visualisation of the majority of hydrogen atoms and accurately depicts
195 the position of each ligand atom. MCRs from ANME-2c and ANME-2d^{O} contain reduced
196 coenzymes trapped in the active site (i.e., CoM-SH and CoB-SH). However, MCR from
197 ANME-2d^{V} exhibits a mixture of ligands. The fit to the electron density was optimal when the
198 model included CoM-SH, CoB-SH, the heterodisulfide, and methyl-CoM (Supplementary Fig.
199 S9). The methyl-CoM, modelled for the first time in an experimental structure, fits a position

200 proposed in a recent molecular dynamics simulation model by Polêto and colleagues with a S-
201 Ni distance of 3.9Å(36). However, due to its low occupancy and the requirement for
202 experimental validation to confirm its existence, we omitted the methyl-CoM from the final
203 deposited model.

204 The ligand-coordinating residues are almost perfectly conserved (Figure 3a-b, Supplementary
205 Fig. S10). In both ANME-2d, a canonical glutamine (position α341 in ANME-2c), proposed
206 to be important to anchor the F_{430}, and juxtaposed to the tyrosine coordinating the CoM thiol
207 (position α342 in ANME-2c) is substituted by a methionine (positions α343 and α346 in
208 ANME-2d^{O} and ANME-2d^{V}, respectively)(36). The substitution does not impact the F_{430}
209 position and provokes few steric displacements in the vicinity (Supplementary Fig. S11).

210 The discovery of a gas channel in the ethane-capturing enzyme prompted us to investigate
211 whether ANME-2 MCR possesses a similar access system for methane. Analysis of the internal
212 cavities in all three models, using CAVER software(37) with a probe radius similar to that of
213 methane, did not reveal tunnels protruding from the active site. In comparison, applying the
214 same parameters to the ECR model from '*Ca.* E. thermophilum' revealed its hydrophobic
215 substrate tunnel. Still, we performed krypton labelling on ANME-2c MCR crystals to verify
216 the existence of an accessory tunnel *via* experimental means. Based on the anomalous signal
217 of the dataset collected at the krypton K-edge, no signals were observed in the active site or
218 tracking in a hydrophobic tunnel (Figure 3c, Supplementary Fig. S12). Krypton atoms are
219 rather positioned on the outer shell of the protein, trapped in hydrophobic pockets, as
220 previously observed for the methanogenic enzyme from *M. marburgensis*(23, 38). The absence
221 of a dedicated gas tunnel connecting the active site to the solvent reinforces the proposed
222 scenario that ethane-specialised homologues evolved this strategy by introducing loop
223 extensions and dedicated PTMs. Enzymes targeting longer alkanes should also have a
224 dedicated entry cavity(19).

225 All three ANME-2 MCRs contained the notably high number of seven PTMs based on the
226 electron density model (Figure 4, Supplementary Fig. S13 and S14). ANME-2c MCR includes
227 the conserved N^1-methylhistidine and thioglycine, the common 5(*S*)-methylarginine, 2(*S*)-
228 methylglutamine, and the rarer S-methylcysteine, didehydroaspartate, and 6-
229 hydroxytryptophane. The same PTMs are present in both ANME-2d MCRs, except for 2(*S*)-
230 methylglutamine. Instead, the histidine 159 from the γ chain harbours a methyl group on its β-
231 carbon in an *S* configuration (i.e., 3(*S*)-methylhistidine). The histidine is canonical and

232 positioned at a distance of 3.5 Å from the F_{430} cofactor, with the atom ND1 forming a hydrogen
233 bond to F_{430}. The modified methyl group is distanced at ~5.7 Å and directed away from the
234 cofactor without disturbing the positioning of surrounding residues (Supplementary Fig. S15).
235 Besides their clear presence in the electron density map, all PTMs could also be confirmed via
236 LC-MS analysis (Supplementary Fig. S16-18).

237

238 Discussion

239 Anaerobic methanotrophic archaea have a significant impact on the global carbon cycle due to
240 their important role as a biological methane filter. The efficiency of their catabolism could be
241 harnessed in microbial-driven technology, as illustrated by electrode-attached ANME-2d
242 producing an electrical current from methane oxidation(14) or as a methane sink in
243 wastewater(39). Therefore, efforts are carried out by the scientific community to decipher their
244 metabolisms. Here, by directly exploiting microbial consortia, we isolated and structurally
245 characterised the key catabolic enzymes from ANME representatives, expanding the available
246 pool of methanotrophic MCR structural models from one to four. Due to their excellent quality,
247 the MCR crystals from ANME-2d provide subatomic resolution, detailing the active site,
248 cofactor, and coenzymes to unprecedented levels. Further structural studies using these models
249 could be conducted to assign protonation states through neutron diffraction or time-resolved
250 crystallography, facilitated by the rapid micro-crystal formation and the high protein yields.
251 This offers prospects for studying the mechanism of methane activation.

252 Compared to active MCR retrieved from hydrogenotrophic methanogens, it is currently not
253 feasible to obtain reactivated ANME enzymes with an *in vivo* approach. Still, our structural
254 insights showed that methane-oxidising MCRs do not contain gas tunnels that connect the
255 solvent with the buried active site, in contrast to the ethane-activating enzyme. Our structural
256 analysis suggests that methane first enters the catalytic site before the heterodisulfide closes
257 the catalytic chamber(19). Such a mechanism is likely to be shared among all ANME MCRs.

258 Structural differences observed between MCRs from ANME-2 and ANME-1 are more likely
259 rooted in their distinct evolutionary histories than in adaptations to specific ecological niches.
260 This is supported by our finding that MCRs from both freshwater and marine ANME-2 archaea
261 are highly conserved despite originating from different environments. According to proposed
262 evolutionary scenarios, methanotrophy in ANME-1 likely evolved from alkanotrophic
263 ancestors (most likely Alkanophaga, however, with an MCR that would originate from

264 *Methanofastidiosa*), while in ANME-2, it emerged from methanogenic lineages
265 (*Methanosarcinales*)(40). These differences suggest that the MCR architectures in ANME-1
266 and ANME-2 arose through convergent evolution, rather than from a shared methanotrophic
267 ancestor. Beyond differences in cofactors (e.g., methylthio-F_{430} versus classic F_{430}) and
268 structural particularities (e.g., presence or absence of a cysteine-rich path), the repertoire of
269 PTMs is largely divergent between clades (Figure 4 and Supplementary Fig. S14). However,
270 three structural positions appear consistently important for methanotrophy: a conserved N^1-
271 methylhistidine, a thioglycine, and a 5(*S*)-methylarginine in ANME-2/methanogens
272 compensated by S-oxymethionine/7-hydroxytryptophan in ANME-1.

273 With seven PTMs, ANME-2 MCRs gather the largest repertoire of modifications reported
274 among methane-metabolising archaea. Notably, the structurally closest related MCR from *M.*
275 *shengliensis* (also belonging to the same order(41)) harbours the most reduced gallery with
276 three PTMs(35). A rational explanation for the great number of PTMs in ANME would be the
277 kinetic limitation of methane activation compared to the methane release reaction. The methane
278 oxidation in MCR has an appK_m value of ≈10 mM (measured with the MCR isoform I of
279 *Methanothermobacter marburgensis*). This strongly limits the catalytic rates of methane
280 activation by ANME at *in situ* conditions, where methane concentrations are often below 1
281 mM. Recent studies suggest that PTMs stabilise the active site and ligands(25, 26), so it might
282 be beneficial for a microbe to invest in equipping its core catabolic machinery to enhance, even
283 slightly, its kinetic properties (i.e., by further decreasing the appK_m). Further studies of other
284 ANME MCRs will be necessary to observe a correlation between the increased amounts of
285 PTMs and methanotrophy. Similarly, future studies could investigate the prevalence of the
286 3(*S*)-methylhistidine and whether it exists in other *Methanosarcinales*. To our knowledge, this
287 is the first report of a 3(*S*)-methylhistidine in a natural protein and the first PTM identified on
288 the γ-chain of any characterised MCR. While the methylation occurs on a residue coordinating
289 the F_{430} cofactor, it appears to have no immediate effect on the surrounding active site, raising
290 questions about its role, in line with the so far mostly unresolved functions of the majority of
291 PTMs observed in MCRs(19, 28). Because all crystallographic structures are mere snapshots
292 of a single state, we cannot exclude a role during catalysis, enzyme assembly, or F_{430}
293 reactivation. Located on a loop at the surface of the γ-subunit, the 3(*S*)-methylhistidine could
294 be installed before the oligomeric assembly by a dedicated methyltransferase. Due to the low
295 nucleophilicity of the β-carbon, the reaction should occur similarly to the installation of a
296 methylarginine (installed by the Mmp10 methyltransferase(26)) or methylglutamine(27) rather

297 than the N^1-methylhistidine, in which an S-adenosylmethionine dependent methyltransferase
298 would substitute a hydrogen of the imidazole ring nitrogen with a methyl group.

299 By revealing the unexpected features of methanotrophic MCRs through accurate models, our
300 work emphasises the need to understand how native systems operate. Highlighting which type
301 of cofactor should be inserted or which PTMs would be appropriate to install would guide the
302 design of efficient heterologous methane capture systems for mitigating greenhouse gas
303 emissions and moving towards a zero-carbon emission society.

304

305 Materials and Methods

306 **Biomass acquisition and microbial enrichments.**

307 ANME-2c cultivation: Sediment was sampled using a multicorer at Amon Mud Volcano, Nile
308 deep-sea fan, Mediterranean Sea at 032° 21.70 N, 031° 23.40 E at a water depth of 1,120 m
309 and 14 °C during NAUTINIL cruise in 2003 with the research vessel RV L'Atalante. Onboard
310 samples were transferred into gas-tight bottles. In the home laboratory, sediment slurries were
311 set up with a synthetic marine sulfate reducer medium at pH 7.4 (Widdel and Bak, 1992(42))
312 and methane headspace at 20 °C. Incubated slurries showed methane-dependent sulfate
313 reduction within a few days. To remove sediment debris, cultures were continuously incubated
314 with methane as the sole electron donor and sulfate as the electron acceptor. The activity-based
315 doubling time for both cultures, monitored by sulfide measurements, was about four to six
316 months. Consecutive dilution and further incubation resulted in debris-free cultures of detached
317 flocks essentially composed of AOM-performing methane-oxidizing archaea and sulfate-
318 reducing bacteria consortia. For more details on the cultivation methods, see Laso-Pérez *et al.*,
319 2018(43).

320 ANME-2d^O bioreactor cultivation of Ooijpolder sample: Granular biomass was obtained from
321 a highly enriched bioreactor culture(33). The culture was maintained in an anaerobic 15 L
322 sequencing fed-batch reactor (30 °C, pH 7.3 ± 0.1 controlled with $KHCO_3$, stirred at 200 rpm,
323 with a working volume between 8 and 11 L). The reactor was continuously sparged with 15
324 mL.min^{-1} CH_4/CO_2 (95:5) and fed with medium (flow rate 2-2.5 L.day^{-1}), as described in Kurth
325 *et al.* 2019(32) with an adaptation of the KH_2PO_4 concentration to 0.05 g L^{-1} and sodium nitrate
326 (15-25 mM) as electron acceptor. Once a day, the biomass was settled for 5 min, after which
327 the excess liquid in the reactor was pumped off to a volume of 8 L.

328 ANME-2d^V bioreactor cultivation of Vercelli rice fields sample: Granular biomass was
329 obtained from a freshwater bioreactor enrichment culture first described by Vaksmaa *et al.*
330 2017(17). The culture was maintained in an anaerobic 15 L sequencing-fed batch reactor (room
331 temperature, pH 7.3 ± 0.1 controlled with $KHCO_3$, stirred at 200 rpm) with a working volume
332 between 8 and 11 L. The reactor was continuously sparged with 10 mL.min^{-1} CH_4/CO_2 (95:5)
333 and fed with medium (flow rate 1.5-2 L.day^{-1}) containing sodium nitrate (5-8 mM). Once a
334 day, the biomass was settled for 5 min, after which the excess liquid in the reactor was pumped
335 off to a volume of 8 L.

336 The medium contained 0.07 g.L^{-1} $MgSO_4.7H_2O$, 0.1 g.L^{-1} $CaCl_2.2H_2O$, 0.05 g.L^{-1} K_2HPO_4,
337 0.5 mL.L^{-1} of trace element solution, 0.3 mL iron solution (54 g.L^{-1} $FeCl_3.6H_2O$ and 114.6
338 g.L^{-1} nitrilotriacetic acid), and 0.1 mL.L^{-1} of Wolin's vitamin solution (DSMZ 141). The trace
339 element solution contained per liter: 0.12 g $CeCl_3.7H_2O$, 0.6 g $CoCl_2.6H_2O$, 4.0 g $CuSO_4$, 0.07
340 g H_3BO_3, 1.0 g $MnCl_2.4H_2O$, 0.35 g $Na_3MoO_4.2H_2O$, 0.1 g $Na_2WO_4.2H_2O$, 0.95 g $NiCl_2.6H_2O$,
341 0.14 g SeO_2, 1.44 g $ZnSO_4.7H_2O$.

342 **Metagenome sequencing**

343 ANME-2c: For DNA extraction, 20 ml of the AMW culture was sampled and pelleted by
344 centrifugation. From the pellet, microbial DNA was extracted using the DNeasy PowerSoil Kit
345 (Qiagen, Venlo, Netherlands) following the supplied protocol. Library preparation and
346 Illumina sequencing (2 x 150 bp reads, 150 million raw reads) were performed at LGC
347 Genomics (Berlin). The metagenomic reads were assembled using SPAdes v. 4.0.0 with default
348 parameters(44) and automatically binned with the software SemiBin (v. 2.1.0) on the *de novo*
349 assembly using the *single_easy_bin* pipeline(45). Three bins affiliated with ANME-2 were
350 obtained according to GTDB (v. 2.1.1) classification(46). Annotation was carried out with
351 prokka v. 1.14.6(47), followed by extraction of the corresponding MCR proteins.

352 ANME-2d: Genomes were retrieved from GTDB-Tk v2.4.0 for ANME-2D^O, '*Ca*.
353 Methanoperedens sp.' BLZ2 under accession number GCA_002487355.1 and ANME-2D^V,
354 '*Ca*. Methanoperedens' Vercelli Strain 1 under accession number GCA_905339155.1. MCR
355 sequences from '*Ca*. Methanoperedens sp.' BLZ2 correspond to NCBI entries
356 WP_097300250.1, WP_097300253.1, and WP_097300251.1 for the α, β, and γ subunits,
357 respectively. MCR sequences from '*Ca*. Methanoperedens' Vercelli Strain 1 correspond to
358 NCBI entries MCX9030096.1, MCX9030093.1, and MCX9030095.1, for the α, β, and γ
359 subunits, respectively.

360 DNA extraction and sequencing of ANME-2d^{O} and ANME-2d^{V} were performed as described
361 previously(48). Microbial taxonomic profiles of the different ANME enrichments were
362 determined using SingleM(49) against the GTDB-Tk database version 2.4.0. Read quality was
363 assessed using FASTQC v0.11.9. The ANME-2c sample consisted of 83 million reads of 150
364 bp, which resulted in a 2367× profile coverage, while the ANME-2d^{O} and ANME-2d^{V} samples
365 consisted of 6.6 and 5.5 million reads of 300 bp, respectively, resulting in 572× and 574×
366 profile coverage.

367 **Sample treatment and lysis**

368 ANME-2c: Two anaerobic 150 mL AOM enrichment cultures were used as starting material.
369 Particles were settled overnight at RT, followed by the removal of ~130 mL of clear
370 supernatant. H_2S in the culture headspace was replaced with N_2 gas before transferring the
371 culture to an anaerobic chamber. Cell lysis and preparation of extracts were performed in a
372 N_2/CO_2 atmosphere (90:10%) at 31 °C. Both samples were pooled and centrifuged at 8,000 ×
373 *g* for 5 min. The supernatant was carefully removed, resulting in a pellet of ~ 3.21 g (wet
374 weight). The aggregates were resuspended in 30 mL IEC-A buffer (50 mM Tricine/NaOH pH
375 8 and 2 mM dithiothreitol (DTT)) and lysed via two rounds of sonication interceded with a
376 French Press treatment at 1,000 PSI (6.895 MPa). The French press cell was flushed with N_2
377 gas before use to ensure anoxic conditions. Unfortunately, 7.5 mL of the lysed sample was lost
378 in the airlock due to an accidental break of the serum flask. The leftover total extract was then
379 diluted to 60 mL with IEC-A, followed by centrifugation at 45,000 × *g* for 30 min at 18 °C. A
380 volume of 100 µL was withdrawn at each step for SDS-PAGE analysis (Supplementary Fig.
381 S2).

382 ANME-2d^{O}: Frozen biomass containing '*Ca.* Methanoperedens sp.' BLZ2 (17.5 g of cells) was
383 transferred to an anaerobic chamber containing an N_2/CO_2 atmosphere (90:10%) and
384 resuspended in 90 mL buffer IEC-A. Cells were first lysed via two rounds of sonication
385 (SONOPULSE Brandelin, 75% power, 30 sec, 1st round: 4 cycles, 2nd round: 3 cycles)
386 interceded with a French Press treatment at 1,000 PSI (6.895 MPa). The French press cell was
387 previously flushed with N_2 to ensure anoxic conditions. After the second round of sonication,
388 the sample was centrifuged at 45,000 × *g* for 30 min at 18 °C. The supernatant was collected
389 and subjected to ultracentrifugation at 100,000 × *g* for 1.5 hours at 4 °C (rotor used: 70Ti,
390 Beckman Coulter). A volume of 100 µL of the total cell extract and soluble fraction was
391 withdrawn for the Bradford assay and SDS-PAGE.

392 ANME-2d^{V}: The frozen biomass (12.47 g) was resuspended in 60 mL buffer IEC-A. Cells were
393 processed the same way as ANME-2d^{O} except for the following variation. The supernatant
394 from ultracentrifugation was sonicated for an additional four cycles, and 40 mL of filtered
395 supernatant was obtained before injection onto the HiTrap Q HP column.

396 **MCR purification**

397 ANME-2c: Protein purification was performed under anoxic conditions in an anaerobic Coy
398 tent with an N_2/H_2 atmosphere (97:3%) at 20 °C under yellow light. Before every injection
399 onto a chromatography column, the sample was filtered using a 0.2 µm nitrocellulose filter
400 (Sartorius, Germany). Proteins were tracked via multi-wavelength absorbance monitoring (λ
401 280, 415, and 550 nm) in combination with SDS-PAGE. The filtered soluble extract (60 mL;
402 20.7 mg protein) was loaded onto a 1 mL HiTrap Q-Sepharose HP column (Cytiva, Munich,
403 Germany) equilibrated with IEC-A. The proteins were eluted with a two-step protocol,
404 reaching 0.5 M and then 1 M at a flow rate of 0.7 mL.min^{-1}. MCR was eluted at 0.5 M NaCl,
405 and the pool (~13 mL) was diluted ~1:4 (protein sample: buffer) with IEC-A buffer. The
406 filtered sample was loaded on a 0.982 mL Mono Q 5/50 column (Cytiva, Munich, Germany).
407 The elution was performed at a gradient of 100 to 700 mM NaCl at 0.5 mL.min^{-1}. The pooled
408 MCR fractions were diluted ~1:4 (protein sample: buffer) with HIC-B buffer (25 mM
409 Tricine/NaOH pH 7.6, 2 M $(NH_4)_2SO_4$, and 2 mM DTT). The pool was filtered and passed on
410 a 1.622 mL Source15ϕ column (Cytiva, Munich, Germany). Proteins were eluted by applying
411 a gradient of 1.5 to 0 M $(NH_4)_2SO_4$ at 0.6 mL.min^{-1}. The final MCR pool was washed by
412 dilution (1:1000) with storage buffer (25 mM Tris/HCl pH 7.6, 10% v/v glycerol, and 2 mM
413 DTT) using a 30 kDa cut-off concentrator to remove salts. Finally, the sample was concentrated
414 to 200 µL. The protein concentration estimated via the Bradford method was 24.6 mg.mL^{-1}.

415 ANME-2d^{O}: Purification was performed under the previously described conditions, and
416 fractions of interest were followed at λ 280 nm. The soluble extract (90 mL at 7.82 mg.mL^{-1})
417 could not be filtered due to the large particulate size and was directly injected into the 10 mL
418 HiTrap Q-Sepharose HP column pre-equilibrated with IEC-A buffer. After washing the
419 column, the elution was performed with a gradient of 0 to 650 mM NaCl for 10 column volumes
420 (CV) at a 2 mL.min^{-1} flow rate. The pool of interest was diluted 1:1 with HIC-B buffer, filtered,
421 and loaded on the 1.622 mL Source 15ϕ column. A gradient from 80% to 0% $(NH_4)_2SO_4$ for
422 10 CV at a 1.5 mL.min^{-1} flow rate was applied. The final MCR fractions were pooled and
423 concentrated on a Vivaspin centrifugation concentrator with a cut-off of 30 kDa. The buffer

424 was exchanged by ultrafiltration for the storage buffer (25 mM Tris/HCl pH 8.0, 10% v/v
425 glycerol, 2 mM DTT, and 100 mM NaCl) containing NaCl to prevent the spontaneous
426 formation of microcrystals. Around 2 mL of purified MCR was recovered at 57 $mg.mL^{-1}$,
427 aliquoted into 50 µL, and stored at 4 °C and −80 °C.

428 ANME-2d^{V}: Purification was performed under the previously described conditions, and
429 fractions of interest were followed at λ 280 nm. The filtered soluble extract (40 mL) was
430 injected into the 10 mL HiTrap Q HP column pre-equilibrated with IEC-A buffer. After
431 washing the column, the elution was performed with a gradient of 0 to 650 mM NaCl for 16
432 column volumes (CV) at a 2 $mL.min^{-1}$ flow rate. The pool of interest was diluted 1:2 (protein
433 sample:buffer) with HIC-B buffer, filtered, and loaded on a 5 ml HP Phenyl Sepharose column.
434 A gradient from 1.3 M to 0 M of $(NH_4)_2SO_4$ for 12 CV at a 1.0 $mL.min^{-1}$ flow rate was applied.
435 The final MCR fractions were pooled and concentrated using a Vivaspin centrifugation
436 concentrator with a 30 kDa cut-off. Ultrafiltration exchanged the buffer for storage buffer.
437 Around 0.35 mL of purified MCR was recovered at 40 $mg.mL^{-1}$ and stored at 4 °C and −80
438 °C.

439 **UV-visible spectrophotometry**

440 UV-visible absorption spectra were recorded using a Cary 60 spectrophotometer (Agilent
441 Technologies, Waldbronn, Germany) on a TrayCell with a 1 mm path length.

442 **Phylogeny analyses**

443 The three MCR subunits from each MAG were concatenated and used to calculate a
444 phylogenetic tree, including the sequences of the studied MCRs from ANME-2c and ANME-
445 2d of this manuscript and the sequences of structural homologues. The concatenated MCR
446 sequences were aligned using MUSCLE v3.8.1551(50). The aligned concatenated sequences
447 were used to calculate a phylogenetic tree with RAxML v.8.2.12(51) using a partition file to
448 calculate differential models for each gene and the following parameters '-m
449 PROTGAMMAAUTO -f a -N autoMRE -k'.

450 **Crystallisation**

451 ANME-2c: The fresh preparation of MCR was immediately crystallised. Crystals were
452 obtained using the sitting drop method on 96-Well MRC 2-Drop Crystallization Plates in
453 polystyrene (SWISSCI, Switzerland), containing 90 µL of crystallisation solution in the
454 reservoir. 0.5 µL protein sample at a concentration of 24.6 $mg.mL^{-1}$ was mixed with 0.5 µL of

455 crystallisation solution. The crystallisation screening was performed by an OryxNano (Douglas
456 Instrument, UK) at 18 °C in a tent filled with 100% N_2. Then, plates were transferred to a Coy
457 tent (N_2/H_2 atmosphere 97:3%) at 20 °C. Crystals were formed over the following days. The
458 most successful conditions were: (A) 30% v/v 2-Methyl-2,4-pentanediol, 100 mM Tris pH 8.5,
459 500 mM NaCl and 8% w/v Polyethylene glycol 8,000, and (B) 30% v/v Polyethylene glycol
460 400, 100 mM HEPES pH 7.5, 200 mM $MgCl_2$.

461 The conditions were replicated on a Junior Clover plate (Jena Bioscience, Germany) under oxic
462 conditions with 90 µL of the crystallisation solution in the reservoir. Crystals with yellow
463 square or rectangular morphology appeared over the next two weeks. The final dataset of
464 ANME-2c MCR was obtained from crystals formed from 2 µL of protein and 2 µL of condition
465 A.

466 ANME-2d^{O}: Following an initial screening on a 96-well MRC 2-Drop Crystallization Plate
467 done aerobically at 18 °C, MCR crystals were reproduced using the sitting drop method on a
468 Junior Clover plate. The best crystals were obtained with a reservoir filled with 100 µL of the
469 following crystallisation solution: 20% w/v polyethylene glycol 3,350, 50 mM Tris pH 8.0 and
470 200 mM potassium nitrate and by spotting 5 µL protein at a concentration of 2.19 $mg.mL^{-1}$
471 with 2 µL crystallisation solution. Thick yellow brick-shaped crystals appeared within 24-48
472 hours.

473 ANME-2d^{V}: Following an initial screening on a 96-well MRC 2-Drop Crystallization Plate
474 done aerobically at 18 °C, MCR crystals were reproduced using the sitting drop method on the
475 Junior Clover plate. Here, the reservoir was filled with 100 µl of 20% w/v Polyethylene glycol
476 3,350 and 200 mM sodium thiocyanate pH 6.9, and the crystallisation well contained 3 µL
477 protein at a concentration of 40 $mg.mL^{-1}$ with 2 µL mother liquor.

478 **Krypton labelling**

479 ANME-2c MCR in solution was shipped to the High-Pressure Freezing Laboratory for
480 Macromolecular Crystallography (HPMX)(52) of the European Synchrotron Radiation Facility
481 (ESRF, Grenoble, France). Crystallisation was repeated using the crystallisation solution from
482 condition B (see crystallisation of ANME-2c MCR) at ambient temperature in an aerobic
483 environment on a Junior Clover plate (Jena Bioscience, Germany). Obtained crystals were used
484 for the krypton-labelling using the pressurisation method. Here, crystals were pressurised at
485 214 bars of krypton for 2 min prior to being flash frozen at cryogenic temperature, still under

486 pressure. X-ray crystallographic data were collected on the beamline ID23-1 (ESRF) at 14.4
487 keV, above the krypton absorption edge.

488 **X-ray data collection, processing, modelling, and validation.**

489 MCR crystals were soaked in the crystallisation solution supplemented with 20% v/v ethylene
490 glycol for ANME-2d^{O} and ANME-2d^{V} for 5-10 seconds before being transferred to liquid
491 nitrogen.

492 X-ray diffraction for ANME-2c crystals was collected at SOLEIL (Source optimisée de lumière
493 d'énergie intermédiaire du LURE) synchrotron, Saint-Aubin, France, at the beamline
494 PROXIMA-1. Crystals for both ANME-2d were collected at the European Synchrotron
495 Radiation Facility (ESRF), Grenoble, France, on the beamline BM07-FIP2. Krypton-derivative
496 ANME-2c crystals were collected at the ESRF on ID23-1 beamline.

497 The datasets were processed and scaled with *autoPROC* (Version 1.0.5, Global Phasing
498 Limited, Cambridge, UK)(53), except for the krypton-derivative sample, which was integrated
499 with XDS and scaled with *aimless* from the CCP4 package. The structures were solved by
500 molecular replacement using *PHASER* from the *PHENIX* package (Version 1.19.2-4158)(54).
501 For molecular replacement, we used an AlphaFold 2(55) model based on the metagenome-
502 derived amino acid sequence for MCR of ANME-2c. The ANME-2c MCR model was used as
503 a template to solve krypton-derivative MCR ANME-2c and as-isolated ANME-2d^{O} MCR
504 datasets. Finally, the ANME-2d^{O} MCR model was used as a template to solve ANME-2d^{V}
505 MCR.

506 All models were then refined with *COOT* (Version 0.8.9.2)(56) and *PHENIX* refine. Because
507 of the high resolution, all atoms were considered anisotropic (except for the krypton-derivative
508 model), and hydrogens were added in riding mode. ANME-2d^{V} MCR was refined with a mix
509 of ligands in the active site, since this resulted in the best fit to the electron density
510 (Supplementary Fig. S9). All models have been deposited with hydrogen atoms modelled on
511 the protein (*e.g.*, not on ligands and solvents).

512 The models were validated by the MolProbity server (http://molprobity.biochem.duke.edu).
513 Figures of MCR structures were generated with PyMOL (V. 2.2.0, Schrödinger, LLC).
514 Sequence alignments were generated with MAFFT 7(57) and visualised with ESPript 3.0(58).
515 Internal tunnels analyses connecting the active site to the surface were performed by CAVER

516 with default parameters and considering a radius of 0.9(37). With these parameters, no tunnels
517 could be detected except for the ECR control.

518 **Mass spectrometry analysis**

519 Purified MCRs in solution was used for liquid chromatography mass spectrometry (LC-MS)
520 analysis to confirm the presence of the PTMs observed in the electron density.

521 The purified proteins were digested after carbamidomethylation with trypsin, chymotrypsin, or
522 elastase at 30 °C in ammonium bicarbonate buffer. In order to obtain many different peptides,
523 sodium lauryl sulphate, sodium deoxycholate, or guanidine hydrochloride were added in
524 various digestion approaches. The duration of incubation with protease was varied from 1.5 to
525 15 hours. In addition, ANME-2c MCR was labeled via vinylpyridine or iodoacetamide. The
526 peptides were then desalted using C18 SPE and measured using LC-MS carried out on an
527 Exploris 480 instrument connected to an Ultimate 3000 RSLC nano and a nanospray flex ion
528 source (all ThermoFisher Scientific, USA). The separating gradient of 60 minutes ran with
529 solvent A, 0.15% formic acid in water, and solvent B, 0.15% formic acid in acetonitrile. The
530 data were recorded in DDA mode and analysed using the Byonic or Proteomediscoverer
531 software and the sequence data files (FASTA).

532 It should be noted that the hydroxytryptophan could not be found reliably with Byonic and
533 often included artificial new adduct masses. Additional analysis with Proteomediscoverer
534 (Sequest) has identified the modified residue reliably in both ANME-2d MCRs.

535

536 Data availability

537 Metagenomic sequences from the Amon Mud Volcano enrichment were deposited under NCBI
538 BioProject ID PRJNA1248948.

539 All models and their structure factors were deposited under the following protein data bank
540 identifiers: 9QR3, MCR ANME-2c; 9QM5, Krypton gassed MCR ANME-2c; 9RQ1, MCR
541 ANME-2d^{O}; 9QQT, MCR ANME-2d^{V}.

542

Acknowledgements

We are thankful to the Max Planck Institute for Marine Microbiology and the Max Planck Society for their continuous support. We thank Christina Probian and Ramona Appel of the Microbial Metabolism laboratory for the technical assistance. We acknowledge the French Biology/Health Panel Review Committee for the provision of synchrotron radiation beamtime at SOLEIL (Saint Aubin, France) on beamline PROXIMA-1 and at the ESRF (Grenoble, France) on beamline BM07-FIP2. BM07-FIP2 is supported by the French ANR PIA3 (France 2030) EquipEx+ project MAGNIFIX under grant agreement ANR-21-ESRE-0011. We acknowledge the ESRF for providing synchrotron radiation beamtime on beamline ID23-1 and access to the HPMX laboratory. T.W. was supported by a European Research Council consolidator grant [Grant number 101125699] and the Max Planck Society. The initial crystallisation screening performed by an OryxNano robot was financed by the Deutsche Forschungsgemeinschaft (DFG) priority programme 1927 Iron-Sulphur for Life [Grant number WA 4053/1-1]. C.U.W. thankfully acknowledges financial support from the Dutch Science Foundation through an NWO-VIDI Talent Grant [Grant number VI.Vidi.223.012] and the SIAM Gravitation Grant [Grant number 024.002.002]. R.L.-P. was funded by a Ramón y Cajal grant (RyC2021-031775-I) from the Spanish Ministerio de Ciencia e Innovación (MCIN/AEI/10.13039/501100011033) and the European Union («NextGenerationEU»/PRTR).

Author contributions

Enrichment of ANME-2c was done by G.W., enrichments of ANME-2d were done by M.W. and C.U.W. Metagenomic data processing for ANME-2c and ANME-2d was done by R.L.-P. and M.W., respectively. Purification and crystallisation of ANME-2c MCR were performed by M.-C.M. and N.V.P. Purification and crystallisation of ANME-2d^{O} MCR was done by P.M. and M.W. Purification and crystallisation of ANME-2d^{V} were done by M.W. and T.W. Data collection was done by S.E., and T.W. Krypton pressurisation were done by S.E. and P.C. X-ray data processing, model refinement and analysis were done by M.-C.M. and model validation by T.W. LC-MS processing and analyses was performed by J.K. The manuscript was written by M.-C.M. and T.W. Manuscript edition and correction were done by all authors.

References

1. Gao YH, Wang Y, Lee HS, Jin PK. Significance of anaerobic oxidation of methane (AOM) in mitigating methane emission from major natural and anthropogenic sources: a review of AOM rates in recent publications. Environ Sci Adv. 2022;1(4):401-25.
2. Segarra KE, Schubotz F, Samarkin V, Yoshinaga MY, Hinrichs KU, Joye SB. High rates of anaerobic methane oxidation in freshwater wetlands reduce potential atmospheric methane emissions. Nat Commun. 2015;6:7477.
3. Boetius A, Ravenschlag K, Schubert CJ, Rickert D, Widdel F, Gieseke A, et al. A marine microbial consortium apparently mediating anaerobic oxidation of methane. Nature. 2000;407(6804):623-6.
4. Timmers PHA, Welte CU, Koehorst JJ, Plugge CM, Jetten MSM, Stams AJM. Reverse methanogenesis and respiration in methanotrophic archaea. Archaea. 2017;2017.
5. Chadwick GL, Skennerton CT, Laso-Pérez R, Leu AO, Speth DR, Yu H, et al. Comparative genomics reveals electron transfer and syntrophic mechanisms differentiating methanotrophic and methanogenic archaea. PLoS Biol. 2022;20(1).
6. Wang Y, Wegener G, Ruff SE, Wang F. Methyl/alkyl-coenzyme M reductase-based anaerobic alkane oxidation in archaea. Environ Microbiol. 2021;23(2):530-41.
7. Wegener G, Krukenberg V, Ruff SE, Kellermann MY, Knittel K. Metabolic capabilities of microorganisms involved in and associated with the anaerobic oxidation of methane. Front Microbiol. 2016;7.
8. Wegener G, Krukenberg V, Riedel D, Tegetmeyer HE, Boetius A. Intercellular wiring enables electron transfer between methanotrophic archaea and bacteria. Nature. 2015;526(7574):587-90.
9. Cai C, Leu AO, Xie GJ, Guo J, Feng Y, Zhao JX, et al. A methanotrophic archaeon couples anaerobic oxidation of methane to Fe(III) reduction. ISME J. 2018;12(8):1929-39.
10. Glodowska M, Welte CU, Kurth JM. Metabolic potential of anaerobic methane oxidizing archaea for a broad spectrum of electron acceptors. Adv Microb Physiol. 2022;80:157-201.
11. Leu AO, Cai C, McIlroy SJ, Southam G, Orphan VJ, Yuan Z, et al. Anaerobic methane oxidation coupled to manganese reduction by members of the *Methanoperedenaceae*. ISME J. 2020;14(4):1030-41.
12. Scheller S, Yu H, Chadwick GL, McGlynn SE, Orphan VJ. Artificial electron acceptors decouple archaeal methane oxidation from sulfate reduction. Science. 2016;351(6274):703-7.
13. Raghoebarsing AA, Pol A, van de Pas-Schoonen KT, Smolders AJP, Ettwig KF, Rijpstra WIC, et al. A microbial consortium couples anaerobic methane oxidation to denitrification. Nature. 2006;440(7086):918-21.
14. Ouboter HT, Mesman R, Sleutels T, Postma J, Wissink M, Jetten MSM, et al. Mechanisms of extracellular electron transfer in anaerobic methanotrophic archaea. Nat Commun. 2024;15(1):1477.
15. Nauhaus K, Albrecht M, Elvert M, Boetius A, Widdel F. *In vitro* cell growth of marine archaeal-bacterial consortia during anaerobic oxidation of methane with sulfate. Environ Microbiol. 2007;9(1):187-96.
16. Holler T, Widdel F, Knittel K, Amann R, Kellermann MY, Hinrichs KU, et al. Thermophilic anaerobic oxidation of methane by marine microbial consortia. ISME J. 2011;5(12):1946-56.
17. Vaksmaa A, Guerrero-Cruz S, van Alen TA, Cremers G, Ettwig KF, Lüke C, et al. Enrichment of anaerobic nitrate-dependent methanotrophic '*Candidatus* Methanoperedens

622 nitroreducens' archaea from an Italian paddy field soil. Appl Microbiol Biotechnol.
623 2017;101(18):7075-84.
624 18. Krüger M, Meyerdierks A, Glöckner FO, Amann R, Widdel F, Kube M, et al. A
625 conspicuous nickel protein in microbial mats that oxidize methane anaerobically. Nature.
626 2003;426(6968):878-81.
627 19. Lemaire ON, Wagner T. A structural view of alkyl-coenzyme M reductases, the first
628 step of alkane anaerobic oxidation catalyzed by archaea. Biochemistry. 2022;61(10):805-21.
629 20. Thauer RK. Methyl (alkyl)-coenzyme M reductases: Nickel F-430-containing enzymes
630 involved in anaerobic methane formation and in anaerobic oxidation of methane or of short
631 chain alkanes. Biochemistry. 2019;58(52):5198-220.
632 21. Scheller S, Goenrich M, Boecher R, Thauer RK, Jaun B. The key nickel enzyme of
633 methanogenesis catalyses the anaerobic oxidation of methane. Nature. 2010;465(7298):606-
634 U97.
635 22. Mayr S, Latkoczy C, Krüger M, Günther D, Shima S, Thauer RK, et al. Structure of an
636 F430 variant from archaea associated with anaerobic oxidation of methane. J Am Chem Soc.
637 2008;130(32):10758-67.
638 23. Hahn CJ, Lemaire ON, Kahnt J, Engilberge S, Wegener G, Wagner T. Crystal structure
639 of a key enzyme for anaerobic ethane activation. Science. 2021;373(6550):118-21.
640 24. Nayak DD, Liu AD, Agrawal N, Rodriguez-Carerro R, Dong SH, Mitchell DA, et al.
641 Functional interactions between posttranslationally modified amino acids of methyl-coenzyme
642 M reductase in *Methanosarcina acetivorans*. PLoS Biol. 2020;18(2).
643 25. Nayak DD, Mahanta N, Mitchell DA, Metcalf WW. Post-translational thioamidation of
644 methyl-coenzyme M reductase, a key enzyme in methanogenic and methanotrophic Archaea.
645 eLife. 2017;6.
646 26. Deobald D, Adrian L, Schöne C, Rother M, Layers G. Identification of a unique radical
647 SAM methyltransferase required for the sp^3-C-methylation of an arginine residue of methyl-
648 coenzyme M reductase. Sci Rep. 2018;8.
649 27. Gagsteiger J, Jahn S, Heidinger L, Gericke L, Andexer JN, Friedrich T, et al. A
650 cobalamin-dependent radical SAM enzyme catalyzes the unique C-methylation of glutamine
651 in methyl-coenzyme M reductase. Angew Chem Int Edit. 2022;61(32).
652 28. Chen H, Gan QL, Fan CG. Methyl-coenzyme M reductase and its post-translational
653 modifications. Front Microbiol. 2020;11.
654 29. Shima S, Krueger M, Weinert T, Demmer U, Kahnt J, Thauer RK, et al. Structure of a
655 methyl-coenzyme M reductase from Black Sea mats that oxidize methane anaerobically.
656 Nature. 2012;481(7379):98-101.
657 30. Shao NN, Fan Y, Chou CW, Yavari S, Williams RV, Amster IJ, et al. Expression of
658 divergent methyl/alkyl coenzyme M reductases from uncultured archaea. Commun Biol.
659 2022;5(1).
660 31. Berger S, Frank J, Dalcin Martins P, Jetten MSM, Welte CU. High-quality draft
661 genome sequence of "*Candidatus* Methanoperedens sp." strain BLZ2, a nitrate-reducing
662 anaerobic methane-oxidizing archaeon enriched in an anoxic bioreactor. Genome Announc.
663 2017;5(46).
664 32. Kurth JM, Smit NT, Berger S, Schouten S, Jetten MSM, Welte CU. Anaerobic
665 methanotrophic archaea of the ANME-2d clade feature lipid composition that differs from
666 other ANME archaea. FEMS Microbiol Ecol. 2019;95(7).
667 33. Berger S, Cabrera-Orefice A, Jetten MSM, Brandt U, Welte CU. Investigation of
668 central energy metabolism-related protein complexes of ANME-2d methanotrophic archaea by
669 complexome profiling. Biochim Biophys Acta Bioenerg. 2021;1862(1):148308.

34. Echeveste Medrano MJ, Leu AO, Pabst M, Lin Y, McIlroy SJ, Tyson GW, et al. Osmoregulation in freshwater anaerobic methane-oxidizing archaea under salt stress. ISME J. 2024;18(1).
35. Kurth JM, Müller MC, Welte CU, Wagner T. Structural insights into the methane-generating enzyme from a methoxydotrophic methanogen reveal a restrained gallery of post-translational modifications. Microorganisms. 2021;9(4).
36. Polêto MD, Allen KD, Lemkul JA. Structural dynamics of the Methyl-coenzyme M reductase active site are influenced by coenzyme F_{430} modifications. Biochemistry. 2024;63(14):1783-94.
37. Chovancova E, Pavelka A, Benes P, Strnad O, Brezovsky J, Kozlikova B, et al. CAVER 3.0: a tool for the analysis of transport pathways in dynamic protein structures. PLoS Comput Biol. 2012;8(10):e1002708.
38. Ohmer CJ, Dasgupta M, Patwardhan A, Bogacz I, Kaminsky C, Doyle MD, et al. XFEL serial crystallography reveals the room temperature structure of methyl-coenzyme M reductase. J Inorg Biochem. 2022;230:111768.
39. van Kessel MA, Stultiens K, Slegers MF, Guerrero Cruz S, Jetten MS, Kartal B, et al. Current perspectives on the application of N-damo and anammox in wastewater treatment. Curr Opin Biotechnol. 2018;50:222-7.
40. Garcia PS, Gribaldo S, Borrel G. Diversity and Evolution of Methane-Related Pathways in Archaea. Annu Rev Microbiol. 2022;76:727-55.
41. Kurth JM, Nobu MK, Tamaki H, de Jonge N, Berger S, Jetten MSM, et al. Methanogenic archaea use a bacteria-like methyltransferase system to demethoxylate aromatic compounds. ISME J. 2021;15(12):3549-65.
42. Widdel F, Bak F. Gram-negative mesophilic sulfate-reducing bacteria. In: Balows A, Trüper HG, Dworkin M, Harder W, Schleifer K-H, editors. The Prokaryotes: A Handbook on the Biology of Bacteria: Ecophysiology, Isolation, Identification, Applications. New York, NY: Springer New York; 1992. p. 3352-78.
43. Laso-Pérez R, Krukenberg V, Musat F, Wegener G. Establishing anaerobic hydrocarbon-degrading enrichment cultures of microorganisms under strictly anoxic conditions. Nat Protoc. 2018;13(6):1310-30.
44. Prjibelski A, Antipov D, Meleshko D, Lapidus A, Korobeynikov A. Using SPAdes De Novo Assembler. Curr Protoc Bioinformatics. 2020;70(1):e102.
45. Pan S, Zhao XM, Coelho LP. SemiBin2: self-supervised contrastive learning leads to better MAGs for short- and long-read sequencing. Bioinformatics. 2023;39(39 Suppl 1):i21-i9.
46. Chaumeil PA, Mussig AJ, Hugenholtz P, Parks DH. GTDB-Tk: A toolkit to classify genomes with the Genome Taxonomy Database. Bioinformatics. 2020;36(6):1925-7.
47. Seemann T. Prokka: rapid prokaryotic genome annotation. Bioinformatics. 2014;30(14):2068-9.
48. Wissink M, Glodowska M, van der Kolk MR, Jetten MSM, Welte CU. Probing denitrifying anaerobic methane oxidation via antimicrobial intervention: implications for innovative wastewater management. Environ Sci Technol. 2024;58(14):6250-7.
49. Woodcroft B, Aroney S, Zhao R, Cunningham M, Mitchell J, Blackall L, et al. SingleM and Sandpiper: Robust microbial taxonomic profiles from metagenomic data. BioRxiv. 2024.
50. Edgar RC. MUSCLE: multiple sequence alignment with high accuracy and high throughput. Nucleic Acids Res. 2004;32(5):1792-7.
51. Stamatakis A. RAxML version 8: a tool for phylogenetic analysis and post-analysis of large phylogenies. Bioinformatics. 2014;30(9):1312-3.

52. Carpentier P, van der Linden P, Mueller-Dieckmann C. The High-Pressure Freezing Laboratory for Macromolecular Crystallography (HPMX), an ancillary tool for the macromolecular crystallography beamlines at the ESRF. Acta Crystallog D. 2024;80(2):80-92.
53. Vonrhein C, Flensburg C, Keller P, Sharff A, Smart O, Paciorek W, et al. Data processing and analysis with the *autoPROC* toolbox. Acta Crystallogr D Struct Biol. 2011;67:293-302.
54. Liebschner D, Afonine PV, Baker ML, Bunkóczi G, Chen VB, Croll TI, et al. Macromolecular structure determination using X-rays, neutrons and electrons: recent developments in *Phenix*. Acta Crystallogr D Struct Biol. 2019;75:861-77.
55. Jumper J, Evans R, Pritzel A, Green T, Figurnov M, Ronneberger O, et al. Highly accurate protein structure prediction with AlphaFold. Nature. 2021;596(7873):583-9.
56. Emsley P, Lohkamp B, Scott WG, Cowtan K. Features and development of *Coot*. Acta Crystallogr D Biol Crystallogr. 2010;66:486-501.
57. Katoh K, Rozewicki J, Yamada KD. MAFFT online service: multiple sequence alignment, interactive sequence choice and visualization. Brief Bioinform. 2019;20(4):1160-6.
58. Robert X, Gouet P. Deciphering key features in protein structures with the new ENDscript server. Nucleic Acids Res. 2014;42(W1):W320-W4.

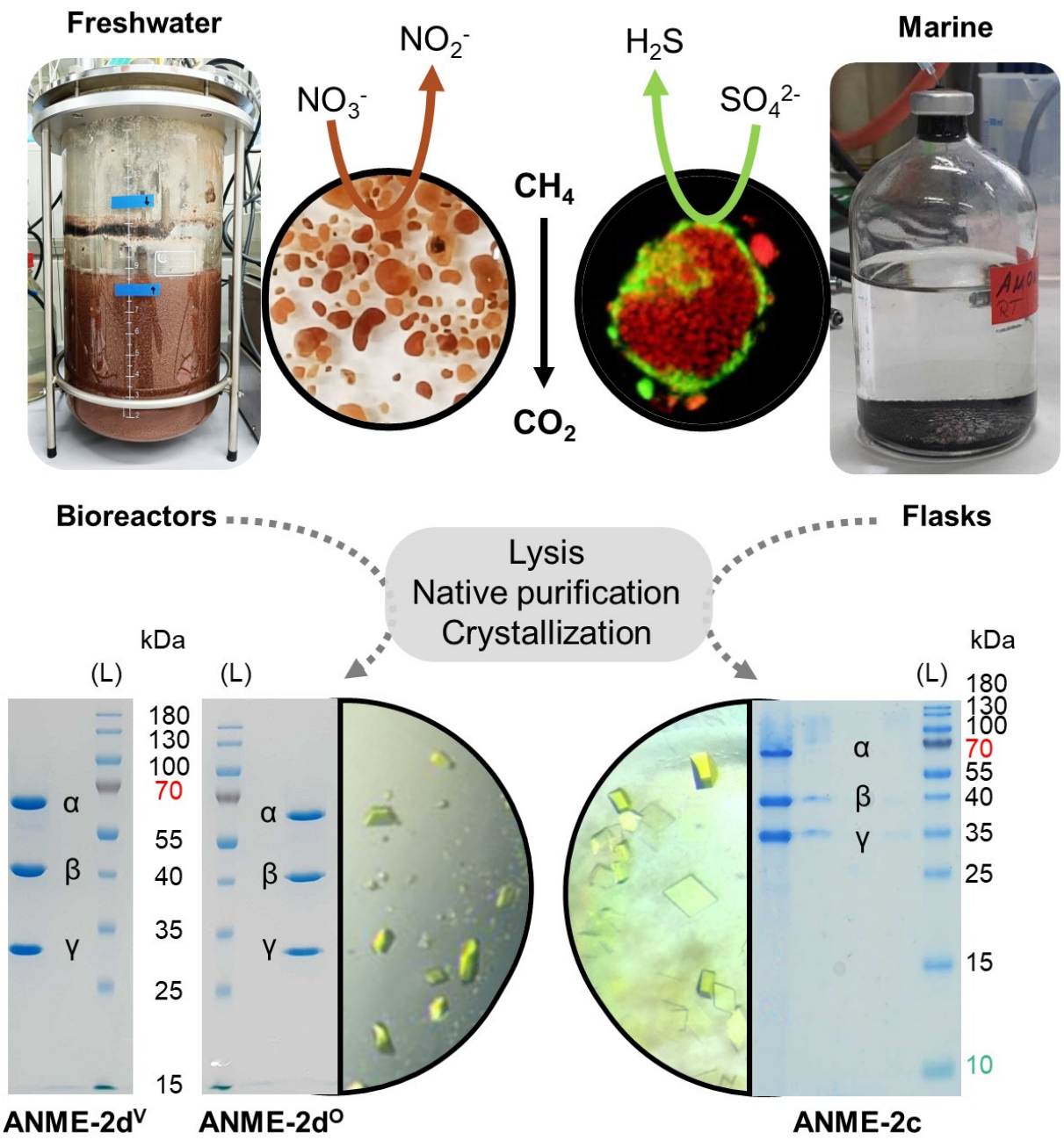

Figure 1. Comparison of the ANME-2 samples investigated in this study and procedure of protein isolation by native purification and crystallisation. Images of the bioreactor and flasks containing the respective freshwater and marine ANME-2 are presented. Close-ups of granular biomass of ANME-2d reducing nitrate and fluorescence *in situ* hybridisation labelled micrographs (7) of the marine methanotrophic consortium (red for the archaeon and green for the sulfate-reducing partner, using specific probes) are shown. Purified MCR fractions are shown on the SDS-PAGE at the bottom of the figure next to the crystals obtained from each sample. For ANME-2c, the sample passed on SDS-PAGE corresponds to dissolved crystals, and a picture of the purification procedure can be examined in Supplementary Fig. S2. L stands for ladder.

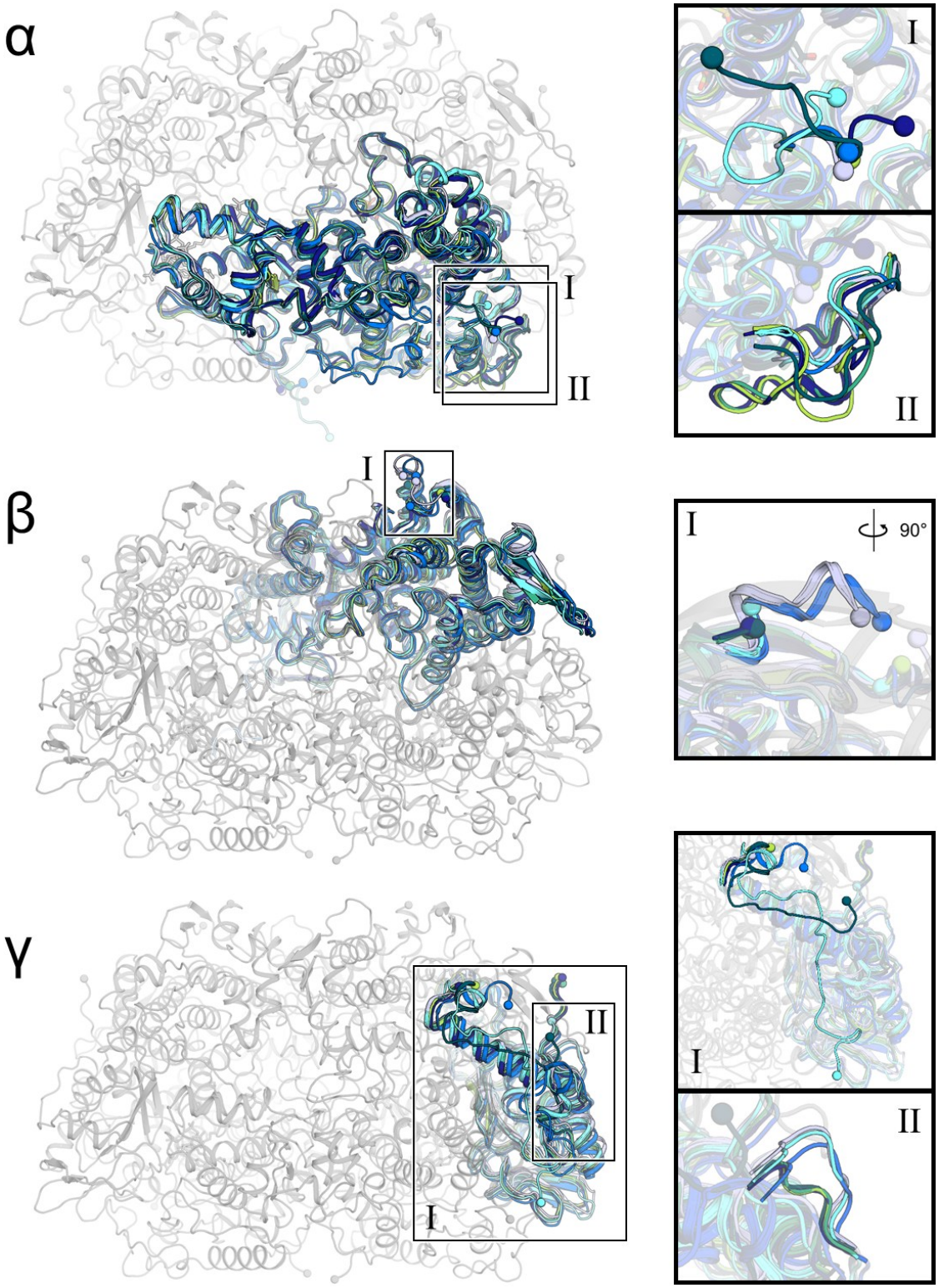

Figure 2. Comparison of ANME-2 MCR structures with previously structurally characterised MCRs. Superposition of the α-, β-, and γ-subunits of MCR. The panels on the right are close-ups of structural deviations. In each panel, the corresponding chain is coloured, while the remaining chains are shown (greyed out) for ANME-2d^{V}. MCR structures are coloured according to the microorganism, with *M. marburgensis* (PDB code: 5A0Y) in light blue, *M. shengliensis* (7NKG) in deep blue, ANME-1 from Black Sea mats (3SQG) in cyan, '*Ca.* E. thermophilum' ECR (7B1S) in marine, ANME-2c in dark green, ANME-2d^{O} in green and ANME-2d^{V} in light green. N- and C-termini are shown as spheres and ligands as sticks.

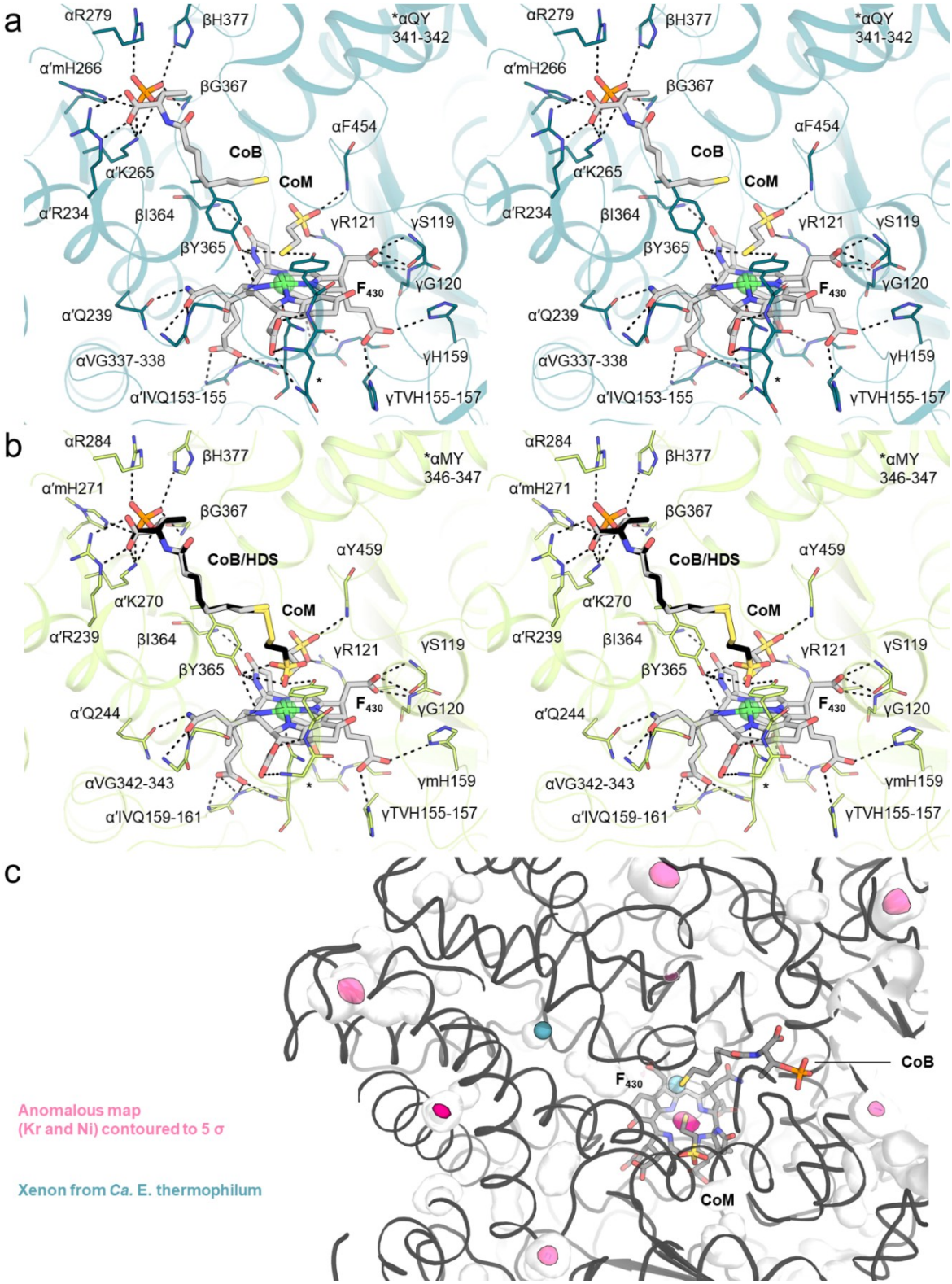

Figure 3. ANME-2 MCR active sites. Stereo-view of the MCR active site in (**a**) ANME-2c and (**b**) ANME-2d^{V}. Interacting residues are shown as lines, and non-interacting side/main chains were omitted. Polar contacts are in black dashes. (**c**) Anomalous map highlights Kr (pink surface). Xe (teal spheres) from '*Ca.* E. thermophilum' (extracted from PDB 7B2C) are superposed. Proteins are in cartoons, and ligands in sticks coloured as follows: red, blue, orange and yellow, for O, N, P and S, respectively.

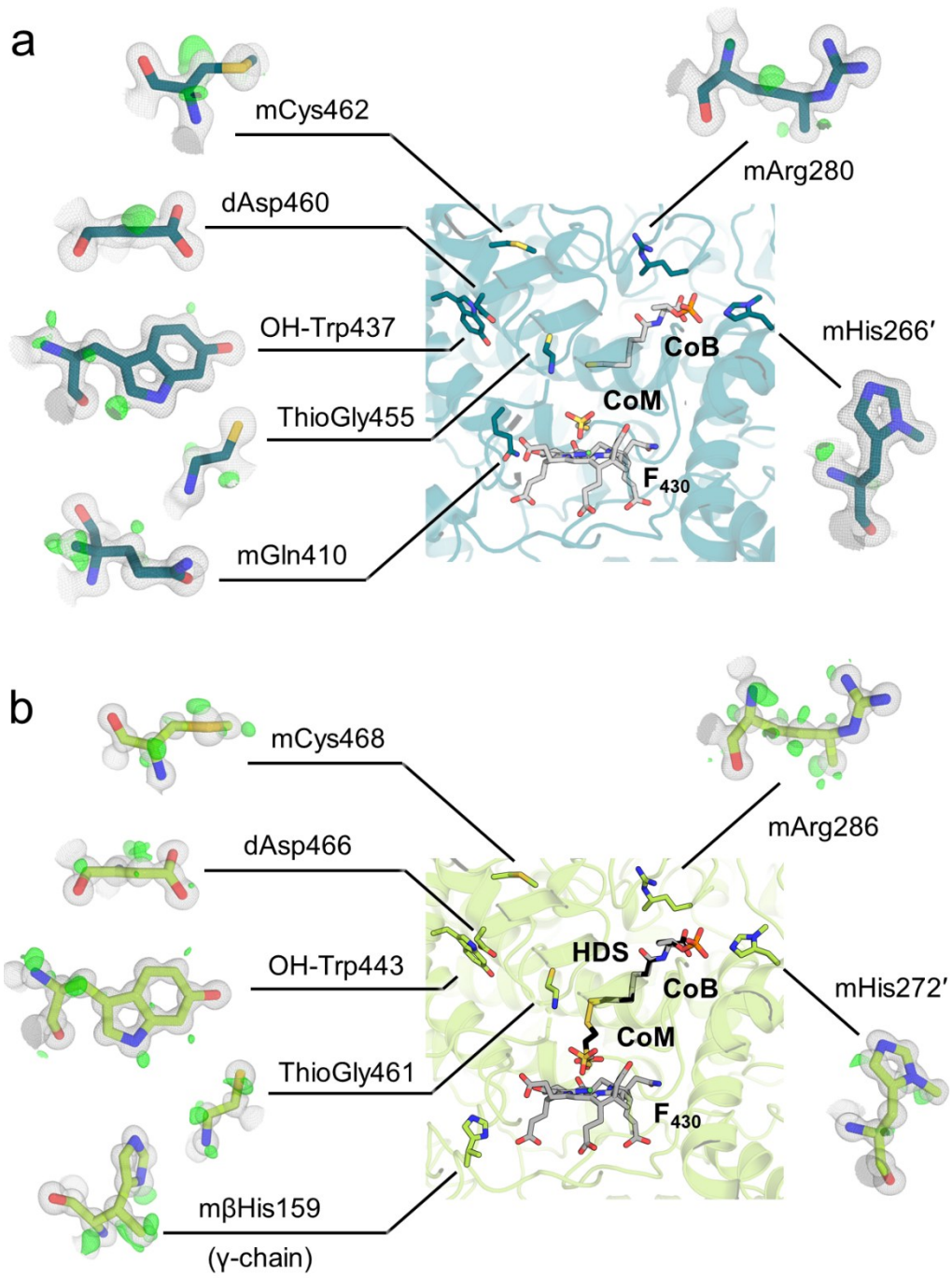

Figure 4. ANME-2 MCR post-translational modifications. PTMs in the active site of (**a**) ANME-2c and (**b**) ANME-2d^{V}. The main chain is shown as a cartoon, with ligands and PTMs shown as sticks with colours according to atoms (red for O, blue for N, orange for P, yellow for S). Close-ups of PTMs flank the central picture, highlighting electron densities. The $2F_o{-}F_c$ map (grey mesh) is contoured at 1 σ, and the $F_o{-}F_c$ map (green mesh) is contoured at 3 σ. The latter highlights the experimental hydrogen positions. The 3(*S*)-methylhistidine is positioned on the γ-chain.

773 **Table 1: X-ray analysis statistics for ANME-2 MCR**

	ANME-2c from microbial enrichment	ANME-2c (Kr pressurised)	ANME-2d^{O} from bioreactor	ANME-2d^{V} from bioreactor
Data collection				
Synchrotron and beamline	SOLEIL, PROXIMA-1	ESRF, ID23-1	ESRF, BM07-FIP2	ESRF, BM07-FIP2
Wavelength (Å)	0.97856	0.86100	0.97980	0.97930
Space group	$P2_1$	$P2_12_12_1$	$P2_1$	$P2_1$
Resolution (Å)	127.16 – 1.35 (1.50 – 1.35)	59.40 – 1.80 (1.83 – 1.80)	76.67 – 0.98 (1.04 − 0.98)	94.91 – 0.98 (1.04 − 0.98)
Cell dimensions				
a, b, c (Å)	156.87, 157.46, 215.42	153.48, 153.67, 212.88	81.58, 189.30, 84.11	81.62, 189.82, 83.93
α, β, γ (°)	90, 90.34, 90	90, 90, 90	90, 114.27, 90	90, 114.36, 90
R_{merge} (%)[a]	16.8 (167.1)	12.7 (162.3)	11.9 (116.8)	7.9 (80.0)
R_{pim} (%)[a]	7.3 (73.7)	5.1 (64.6)	4.5 (46.8)	3.0 (32.0)
$CC_{1/2}$ [a]	0.991 (0.560)	0.999 (0.768)	0.996 (0.667)	0.998 (0.754)
I/σ_I[a]	6.6 (1.6)	14.1 (1.8)	9.4 (1.7)	13.0 (1.9)
Spherical completeness[a]	66.2 (12.2)	100.0 (100.0)	84.4 (24.4)	74.7 (23.5)
Ellipsoidal completeness[a]	96.2 (66.6)	/	96.5 (70.9)	83.9 (62.6)
Redundancy[a]	6.3 (6.0)	13.8 (14.2)	7.8 (7.1)	7.6 (7.0)
Nr. unique reflections[a]	1,527,343 (76,367)	461,593 (22,707)	1,130,261 (56,513)	996,827 (49,841)
Refinement				
Resolution (Å)	98.93 – 1.34	54.30-1.80	41.78 – 0.98	41.72 – 0.98
Number of reflections	1,527,210	461,298	1,130,120	988,481
R_{work}/R_{free}[b] (%)	11.24/14.71	12.93/15.52	10.25/11.76	12.96/14.81
Number of atoms				
Protein	152,558	75,375	39,210	39,298
Ligands/ions	1,328	1,000	406	473
Solvent	9,812	4,293	3,419	3,293
Mean B-value (Å^2)	15.77	29.30	10.72	10.03
Molprobity clash score	0.99	1.50	0.60	0.45
Ramachandran plot				
Favoured regions (%)	97.33	97.11	97.16	97.08
Outlier regions (%)	0.07	0.08	0.08	0.08
rmsd[c] bond lengths (Å)	0.010	0.009	0.010	0.011
rmsd[c] bond angles (°)	1.247	1.170	1.341	1.382
PDB code	9QR3	9QM5	9RQ1	9QQT

774 [a] Values relative to the highest resolution shell are within parentheses. [b] Rfree was calculated
775 as the Rwork for 5% of the reflections that were not included in the refinement. [c] rmsd, root
776 mean square deviation.